Melting of bridgmanite under hydrous shallow lower mantle conditions

George Amulele[1]

Shun-ichiro Karato[2]

Jennifer Girard[2]

[1]: Department of Earth, Environmental, and Planetary Sciences, Case Western Reserve University, 10900 Euclid Avenue, Cleveland, OH 44106

[2]: Department of Earth and Planetary Sciences, Yale University, New Haven CT 06520

To be submitted to Journal of Geophysical Research

Abstract

High pressure and temperature experiments were carried out on bridgmanite under the hydrous shallow lower mantle conditions (24 – 25 GPa and 1673 – 1873 K with 5 – 10 wt. % of water in the starting material). Bridgmanite investigated include $MgSiO_3$, $(Mg, Fe)SiO_3$, $(Mg, Al, Si)O_3$ and $(Mg, Fe, Al, Si)O_3$. Melting was observed in all runs. The water content of the melt was estimated from the measurements of the void space using the equation of state of H_2O that occupies the void space and agree reasonably well with the initial water content. Melt is enriched in FeO/MgO and Al_2O_3/SiO_2 compared to the starting materials. As a consequence, the residual solids contain a substantial amount of stishovite particularly for the high FeO/MgO and Al_2O_3/SiO_2 starting materials. Stishovite-rich materials will cause seismic scattering when they are transported to ~1100 km depth where stishovite shows anomalous elastic behavior. The water content in the residual solids was measured by the FTIR and is 50 – 70 ppm wt. in bridgmanite and 26 – 670 ppm wt. in stishovite, depending on the starting composition. However, bridgmanites in these samples contain inclusions of superhydrous phase B. If these inclusions were formed during cooling, water content in bridgmanite co-existing with hydrous melt would be 1000-1500 wt ppm that agrees with the previous experimental results on inclusion-free bridgmanite and with a theoretical study. Some implications of these results are discussed including the nature of chemical evolution associated with melting in the shallow lower mantle.

Plain Language Summary

Melting is a major process by which Earth evolves chemically. However, the consequence of melting is not well understood under the deep mantle conditions. This study focuses on melting under the shallow lower mantle conditions that occurs with the help of water. Nature of water distribution between the melt and remaining solids was studied using new approaches. We discovered that when melting occurs for a material with composition similar to oceanic crust, the residual solid is nearly completely stishovite (SiO_2). Stishovite shows anomalous elastic properties at ~1100 km depth. Observed strong seismic scattering in this depth range might be due to the presence of stishovite-rich materials formed by melting in the lower mantle.

Introduction

Due to the large contrast in the solubility of water (hydrogen) between lower mantle minerals and transition zone minerals, it is likely that partial melting occurs in the lower mantle if a substantial amount of water (and other volatiles) is present in the lower mantle (e.g., (Ohtani et al., 2004)). (Liu et al., 2016, 2018; Schmandt et al., 2014) reported seismological observations showing a velocity drop (from the shallow to the deep mantle) at around ~750 km and suggested that this velocity drop might be caused by partial melting caused by the transport of water-rich materials from the transition zone.

Although there have been previous studies on melting in the shallow lower mantle (e.g., (Boujibar et al., 2016; Corgne et al., 2005; Ito et al., 2004; Ito and Takahashi, 1987; Kawamoto, 2004; Litasov and Ohtani, 2002; Nakajima et al., 2019; Panero et al., 2020)), the conditions and the consequence of melting on the composition of the melt and the residual solids are poorly

constrained particularly under the hydrous conditions. The composition of the melt (and the residual solid minerals) is important for two reasons. First, the compositional change upon melting controls the way in which Earth evolves chemically and also the contrast in the water content between the melt and the co-existing solids determines the critical amount of water under which melting occurs. Second, the composition of the melt relative to that of the co-existing minerals has a large influence on the density contrast between them that controls the direction to which melt is transported. Particularly important is the contrast in the concentration of Fe and H in the melt and co-existing solids. However, in contrast to extensive studies on the Fe partitioning between the melt and the co-existing solids (e.g., (Irifune et al., 2010; Nishiyama and Yagi, 2003; Nomura et al., 2011; Wood, 2000)), less studies have been made on water (hydrogen) partitioning and large discrepancies remain on the water partitioning between the melt and the solids under the lower mantle conditions.

The main reason for the poor constraints on partitioning of water (hydrogen) is the difficulties in determining the water content in both melts and solids formed under the lower mantle conditions. Melts formed under the lower mantle conditions are unquenchable and there has been no well-established method to determine the water content of these melts. A commonly used practice is to assume that less than 100% of compositional measurements by EPMA (electron-probe micro-analyzer) correspond to the water content. For example, if the EPMA analysis gives 70% total, it is often assumed that water content is 30% (e.g., (Hirschmann et al., 2009; Nakajima et al., 2019)). The physical basis for this method is unclear because the density of void space is different from the rest. Also, the measurement of water (hydrogen) content in a mineral is not trivial. There is a wide range of reports for the water solubility in bridgmanite (e.g., (Bolfan-Casanova et al., 2003; Fu et al., 2019; Litasov et al., 2003; Meade et al., 1994;

Murakami et al., 2002; Panero et al., 2015)). The reason for this large discrepancy is not well understood but it is partly caused by the influence of inclusions (e.g., (Bolfan-Casanova et al., 2003; Fu et al., 2019; Schmandt et al., 2014)). A recent work by (Fu et al., 2019) on inclusion-free (Al, Fe)-bearing bridgmanite single crystal, grown from hydrous melt, shows large water solubility (~1000 ppm wt. water), under the shallow lower mantle conditions.

The main purpose of this study was to investigate the compositions of melts and co-existing solid minerals formed by hydrous melting under the shallow lower mantle conditions with the emphasis on those of Fe and H.

Experimental Procedure

In this study, we focus on the melting behavior of bridgmanite. We synthesized several hydrous compositions of bridgmanite. For hydrous $MgSiO_3$, we used MgO, SiO_2 and $Mg(OH)_2$ oxide starting materials whereas for Al- and Fe-bearing $MgSiO_3$ bridgmanite were synthesized by adding appropriate amounts of Al_2O_3 and FeO (**Table 1**). All the oxides used had purities of 99.99%. Oxide powders were mixed and ground by grinding the mixture in an agate mortar to make nearly homogenous mixture of fine powders (typical grain size was less than 1μm). A fine-grained mixture was loaded and sealed in a platinum capsule (we did some experiments with Fe-Pt capsule to test the degree of Fe loss). A 1000-ton Kawai type multi-anvil press was used for these experiments. A sample assembly was compressed to pressures of ~25 GPa and annealed at a temperature of ~1873K for 3-5 hours. The pressure was estimated from the load, based on the calibration using the phase transformation of majorite to bridgmanite at 1600^{o}C. Temperatures were measured using W-5/26% Re thermocouple wire. The uncertainties in pressure estimate are 0.5 GPa, and that of temperature are 100^{o}C.

After annealing, the heater was shut-off and the pressure was slowly reduced (2.0 GPa/hour). After shutting off the furnace, temperature drops from 1600^{o}C to 1000^{o}C in ~10 seconds. The samples were polished down to ~200 μm and Raman spectroscopy was carried out to determine the phases present. FTIR spectra were then recorded on the solid phases using a Varian FTIR spectrometer with an internal IR source. Scanning electron microscopy (SEM) as well as electron microprobe analyses (EPMA) were also carried out to determine the compositions of both the synthesized products.

Results

Under the current experimental conditions, melts are not quenchable. However, the remnant of melt can be identified unambiguously from the texture (**Figure 1, 2 and 4**), where we observed remnant of melt, in the central part of the capsule. We observed remnant of melt in all the samples investigated in this study. The temperature gradients generated from the design of the assemblies used resulted in the segregation of quenched liquids in the highest temperature regions within the capsule. Phase separation between bridgmanite and stishovite was also observed. This was also observed in diamond anvil melting experiments (Baron et al., 2017).

The left-hand side of **Figure 1** shows a back-scattered image from SEM on a polished MgO-SiO_2-FeO-H_2O system containing 10% wt. H_2O in the starting mixture (K1157). We estimated the melt fraction, *F*, by successively polishing the sample capsule and calculating the melt area at each step of the polish. The samples were first sectioned and after taking optical images they were polished to roughly 200 μm and optical images taken again. This procedure was repeated several time for the entire sample. The areas of the melt and solid phases were calculated from the optical images using an imaging software (ImageJ), and the respective

volume of each phase calculated using the thickness that was polished off (200 μm). From these, the overall melt and solid volume were then estimated. **Figure 2** shows an example of this procedure for sample K1217, where the sample thicknesses at each stage of the polish are included. *F* was estimated to be about 40% (± 5 %), in this case.

Raman spectroscopy measurement

In the solid part (judged from the texture), several minerals were identified including bridgmanite, stishovite and super hydrous phase B (**Table 2**). In the run without Fe, only bridgmanite and melt were formed. When the starting compositions contain Fe and Al, stishovite is observed. In the case where the Fe content was 5 wt. %, only stishovite is formed (**Figure 1**, Right). Raman spectra on pure $MgSiO_3$-bridgmanite showed strong clean peaks identifiable to the mineral. The $MgSiO_3$-bridgmanite synthesized with Al also showed the same Raman peaks with an additional peak at 1096 cm^{-1} at some locations. This peak is identified with superhydrous phase B (**Figure 3**, left) (Koch-Muller et al., 2005; Liu et al., 2002). The superhydrous phase B is observed inside bridgmanite (but not stishovite) as small inclusions in the optical micrograph (**Figure 4**). The origin of this phase will be discussed in relation to the interpretation of FTIR observations. **Figure 5** summarizes the observed phases in the residual solids. Volume fraction of bridgmanite and stishovite depends on Al_2O_3 and FeO content: fraction of stishovite increases as $Al_2O_3/(Al_2O_3 + SiO_2)$ and $FeO/(FeO + MgO)$ increase. In case of $Al_2O_3/(Al_2O_3 + SiO_2) = 0.09$ and $FeO/(FeO + MgO) = 0.19$, the residual material is pure stishovite.

Electron microprobe analysis

Quantitative electron microprobe analysis of both the solid and melt parts of the run products was carried out on all samples. Measurements were made using a 15 KeV acceleration voltage with 30 μm diameter defocused beam. The total of EPMA analyses of the "melt" part yield 50 - 70 % due to the presence of void space (**Table 2**). The (Mg + Fe)/Si molar ratio of the melt ranges from 2.0 – 4.1, up from an initial value of ~1, thus the melt is more mafic than the bridgmanite crystals. The partitioning of Fe is also strongly dependent of Al concentration. The (Mg + Fe)/Si molar ratio in Al-free bridgmanite ((Mg, Fe)SiO_3 composition) increases to 2.7 from ~2 indicating that Al increases the partition of Fe into the melt.

We define the partition coefficients of Fe and Si between the mineral (bridgmanite) and melt by $K_D^{Fe} = \frac{(Fe/Mg)_{mineral}}{(Fe/Mg)_{melt}}$ and $K_D^{Si} = \frac{(Si/Mg)_{mineral}}{(Si/Mg)_{melt}}$, respectively where concentration is in the molar fraction (mineral in this case is bridgmanite). Our measurements show that K_D^{Fe} is 1.05 (in K1161), approximately a factor of 4 larger than the Al-free, Fe-bearing bridgmanite (K_D^{Fe} = 0.25) (in K1157). This result is qualitatively consistent with previous melting experiments on dry Fe- and Al-bearing bridgmanite that suggests that Al enhances Fe partitioning into bridgmanite (Boujibar et al., 2016; Corgne et al., 2005; Ito et al., 2004).

Estimating the water content in the melt

Because the melt produced in these experiments were not quenched to a glass, water content cannot be directly determined from the sample. Rather, the "melt" in the recovered sample is made of small crystals and voids. We interpret that these small crystals were formed during cooling, and voids are the space that were filled with the volatiles (water in this case) that was present in the melt but expelled from the melt during crystallization. In this model, the plausible processes to form such a texture are as follows: (1) Upon cooling at high pressure,

crystals are formed from the hydrous melt. Because these crystals have low water solubility, the water content in the melt increases. (2) With further cooling, the water content in the melt will exceed the solubility limit and water-filled voids will be formed. When temperature reaches room temperature, crystallization is completed and the regions that were originally filled with the melt are now filled with small crystals and a void pace filled by water at a given pressure and room temperature. (3) Now at room temperature, we reduce pressure. During the isothermal pressure reduction, the volume of water will change but some elastic relaxation will occur that modifies the volume of voids. (4) When a capsule is opened, water will evaporate and the void space will be left.

Therefore, in order to estimate the water content in the melt from the microstructure of a recovered sample containing crystals and voids, one needs to measure the volume fraction of voids and the mass of water that filled the voids. Images of the regions containing small crystals and voids (regions that were melt at high pressure and temperature) were collected by scanning electron microscopy (SEM) then analyzed using ImageJ to estimate the porosity (volume fraction of void space) in the melt. **Figure 6** shows examples of SEM images with different starting compositions alongside their digitized images that were used. As shown in **Figure 6** SEM image show solid region and void region with different grayness. To separate void space and solid space, we convert the gray image into a black and white (binary) image in which black is the void and white is the solid. This conversion assumes some threshold value. We explored various threshold values to find optimum threshold value for which uncertainties in the estimated volumes are less than ~5%.

The mass of water that occupied the void space was estimated using the equation of state of water (Hemley et al., 1987). The simplest assumption is that the pressure of water in the void

198 space in the recovered sample is room pressure. This would be the case when the void space is
199 connected. In this case, the mass of water can be estimated by the specific volume of water at
200 ambient condition. However, when void space occurs as isolated inclusions, then the water in the
201 void space could have a higher pressure. Consequently, we have considered a range of pressure
202 of water in the void space, from room pressure to the maximum pressure during an experiment
203 (24 – 25 GPa). In these calculations, the equation of state of water determined by (Hemley et al.,
204 1987) was used (**Figure 7(a)**). The volume of voids estimated on the recovered and polished
205 samples may not be exactly the same as the volume of voids in the sample at room temperature
206 and pressure in the sample before polishing if the pressure of water in the void was high.
207 However, the difference in the volume of voids is small, less than 10%, because this volume
208 change occurs by the elastic deformation of minerals surrounding the voids. The water content in
209 the sample estimated from this method is compared to the initial water content of the sample
210 (**Figure 7, Table 3**).
211
212 ***Water content measurement in minerals***
213 A summary of the infrared absorption peaks observed in the different compositions of
214 bridgmanite is given in **Table 4**. FTIR measurements of pure $MgSiO_3$-bridgmanite at ambient
215 pressure showed a dominant absorption peak at 3446 cm^{-1} (**Figure 8(a)**). Calculation of the
216 water content on this spectrum using the Paterson's equation (Paterson, 1982) gave a value of 70
217 ppm wt. % H_2O. This value is of the same order as that determined by (Meade et al., 1994).
218 FTIR spectra of the solubility in Al-bearing $MgSiO_3$ bridgmanite was dominated by peaks at
219 3346, 3405 and 3695 cm^{-1} wavenumbers. They are likely attributed to superhydrous phase B
220 inclusions (Cynn et al., 1996), while the peak at 3695 cm^{-1} may also be attributed to brucite

(Braterman and Cygan, 2006; de Oliveira and Hase, 2001), (**Figure 8(b)**). Quantification of water in this sample was estimated by assuming that water in superhydrous phase B was initially in bridgmanite. The volume fraction of superhydrous phase B in the quenched sample is estimated to be about 2-3 vol. % (using **Figure 4**). Given that under saturation conditions superhydrous phase B contains about 5 - 6 wt. % water (Bolfan-Casanova et al., 2003; Ohtani, 2005), we can therefore approximate the initial amount of water in the bridgmanite phase to be about 1000 - 1500 ppm wt. water.

Bolfan-Casanova et al. (Bolfan-Casanova et al., 2003)'s also showed that infrared absorption for Al-bearing bridgmanite was dominated by spectra from superhydrous phase B inclusions, and when they removed water in superhydrous phase B, they obtained essentially no detectable water (hydrogen). In contrast, (Litasov et al., 2003) synthesized inclusion free Al-bearing bridgmanite (4 - 7 wt. % Al_2O_3) and determined the water content in the bridgmanite to be 1000 – 1500 ppm wt. water with a major broad band at 3448 cm^{-1}. (Fu et al., 2019) have also determined the water concentration in (Al, Fe)-bearing bridgmanite, where they determined 1020 ppm wt. water in single crystal, inclusion-free bridgmanite, grown from hydrous melt. They observed two FTIR water absorption peaks at 3230 cm^{-1} and 3460 cm^{-1} wavenumbers.

In FeO bearing but Al-free sample (K1157), we observed both bridgmanite and stishovite in the solid phase. Stishovite was mostly located at the boundary between the bridgmanite and melt. No inclusions of superhydrous phase B were seen in this composition. FTIR measurement of water solubility was made, separately for stishovite and bridgmanite phases (**Figure 8(c)**). Absorption peaks in stishovite were observed at 3113, 3238, and 3311 cm^{-1} those agree with the previous report (Pawley et al., 1993), and give a water content of 26 wt. ppm H_2O after subtraction of the baseline. Meanwhile absorption peaks in bridgmanite were observed at 3296

and 3394 cm^{-1} and gave a total water content of 44 wt. ppm H_2O. Both spectra show a peak at 3687 cm^{-1} similar to the OH absorption peak in $Mg(OH)_2$. (Bolfan-Casanova et al., 2003) report only one absorption peak at 3388 cm^{-1} in a (Mg, Fe)SiO_3 bridgmanite sample that amounts to a water content of 2 wt. ppm H_2O.

Several bridgmanite compositions containing both iron and aluminum were also investigated. These are shown in **Table 1**. For the same conditions of pressure and temperature experiment K1161 produced bridgmanite, stishovite and melt in the assemblage while K1182, K1217 and K1222 produced both stishovite and melt with no trace of bridgmanite phase (K1182, **Figure 1**, Right). FTIR absorption peaks observed in K1161 are consistent with those seen in (Mg, Fe)SiO_3 and (Mg, Al)SiO_3 compositions for both the bridgmanite and stishovite phases (**Figure 8(d)**). The absorption peaks at 3242 cm^{-1} and 3479 cm^{-1} are consistent with those observed by (Fu et al., 2019), at 3230 cm^{-1} and 3460 cm^{-1}, respectively. In the experiments where only stishovite and melt were observed, the water solubility peaks measured in the stishovite phase corresponds to absorption peaks at 2661 and 3128 cm^{-1} and is about 670 wt. ppm H_2O (**Figure 8(e)**). This is an order of magnitude higher than that measured in the stishovite produced where no aluminum was present in the starting composition**.**

Discussion

Fe loss

All experiments were carried out using platinum as a capsule material. When studying systems containing iron, usually some iron is lost to the capsule material, hence iron loss must be examined. This is why numerous investigations have been carried out so as to minimize Fe loss

by alloying the platinum capsule material with iron (Balta et al., 2011; Grove, 1981; Gudmundsson and Holloway, 1993; Kessel et al., 2001; Vanderlaan and Vangroos, 1991).

Surprisingly, in our experiments that contained Fe in the starting composition, we did not find any detectable Fe in the Pt capsules by the EPMA. Composition profiles measured across the thickness of the capsule of the polished samples yielded no Fe (less than the detectability, ~0.1 wt. %). Contrary to the Fe loss to a capsule, diffusion of Fe into the sample from the capsule was observed when we used a Pt-Fe alloy capsule. This was confirmed by mass balance analysis when we considered the amount of Fe in the starting composition as well as those measured in the solid and melt phases. We interpret that the cause of little Fe loss to a Pt capsule is due to high oxygen fugacity in our sample assembly due to the presence of a large amount of water (according to (Rubie et al., 1993), the solubility of Fe in Pt decreases with oxygen fugacity).

Further, the mass balance analysis confirmed a melt fraction of 36 - 40 % that is consistent with the estimation of melt fraction obtained from the successive polishing of the capsule and calculating the melt fraction using image analysis discussed earlier. The mass balance results for sample K1157 are shown in **Table 5**.

A comparison to previous method of water content estimate of unquenchable melts

Figure 7(a) shows a comparison of the water content of the recovered sample (estimated from the water content in the unquenchable melt as described before) and the water content of the starting materials. The agreement is reasonable, and we conclude that (i) not much water escaped from the sample during an experiment, and (ii) our new method of estimating water content in an unquenchable melt is valid.

There is no well-established method to estimate the water content of melt when melt cannot be quenched to a glass. A commonly used practice of estimating volatiles is to identify the deficit of EPMA measurements from 100% (e.g., (Hirschmann et al., 2009), see also (Nakajima et al., 2019)). We compare the results of estimates of water content based on the void space and equation of state with the results of this conventional method (**Figure 7(b)**). It is seen that the conventional method gives systematically higher water content, and that in many cases, the water content estimated by this conventional method exceeds the water content of the starting material indicating that this method is not appropriate. This is most likely caused by the fact that the density of materials (water) filling the void space is substantially less than the density of the rest of a sample. The difference in the estimated water content is very large and it has an important implication for the density of the melt.

However, our method also has a large uncertainty regarding the physical status of the void space during depressurization.

A comparison to the previous studies on hydrogen dissolution in lower mantle minerals

There has been a large discrepancy in the water solubility in bridgmanite in previous studies (e.g., (Bolfan-Casanova et al., 2003; Fu et al., 2019; Litasov et al., 2003; Litasov et al., 2007)). One plausible cause for this discrepancy is the presence of water-rich "inclusions". For instance, (Schmandt et al., 2014) reported that water-rich melt inclusions in bridgmanite caused a broad absorption similar to those observed by (Bolfan-Casanova et al., 2003; Murakami et al., 2002), and suggested that a large water solubility reported by (Murakami et al., 2002) is caused by these inclusions. Similarly, water-rich inclusions such as superhydrous phase B (in cases of bridgmanite) (Bolfan-Casanova et al., 2003) or brucite (in case of (Mg, Fe)O) (Bolfan-Casanova

et al., 2002) could lead to high solubility. Our results on water content in bridgmanite are similar to those studies where some superhydrous phase B was reported.

In contrast to these results, (Fu et al., 2019) reported a substantially higher amount of water solubility in inclusion-free bridgmanite synthesized from a hydrous melt under the shallow lower mantle conditions (P = 24 GPa, T = 1873 K) (see also (Litasov et al., 2003)). Since inclusions of hydrous phase such as superhydrous phase B are often observed in our study and most previous studies but not in (Fu et al., 2019) and (Litasov et al., 2003), it is likely that this difference is caused by inclusions. However, the reason why inclusions of superhydrous phase B cause small water content in bridgmanite is not clear. Note that superhydrous phase B is not stable under the conditions from which samples are annealed (P = 25 GPa and T = 1873 K). Consequently, it is likely that those inclusions were formed during quenching, and if this is the case, water (hydrogen) content in these inclusions should not be subtracted when calculating the water solubility in bridgmanite. Indeed, if we use diffusion coefficient of hydrogen in olivine as a guide (e.g., (Kohlstedt and Mackwell, 1998)), we find that time needed to diffuse hydrogen to form inclusions of superhydrous phase B with ~10 micron distance is less than one second.

Indeed a computational study by (Hernandez et al., 2013) on (Fe and Al free bridgmanite at the similar P-T conditions reported similar water solubility (1000 ppm wt), suggesting that the true water solubility in bridgmanite is of the order of 1000 ppm wt but the effect of Fe and Al should be explored in more detail.

We also note that because our results suggest that hydrogen location in bridgmanite (and other minerals) is unquenchable, interpretation of the peak position and the breadth of infrared absorption is complicated. For example, hydrogen location (crystallographic site) may change during cooling, and hydrogen may form hydrous minerals such as superhydrous phase B or small

water bubbles. A wide variety of observed infrared spectra likely reflects different processes during cooling in addition to the variety of crystallographic site where hydrogen may be located at high pressure and temperatures. It would be interesting to explore the role of cooling processes on the nature of infrared absorption to understand the role of cooling processes.

A comparison to the previous studies on the major element (Fe and Al) partitioning

We now compare the results on major element partitioning between bridgmanite and co-exiting melt of our experiments. The previous results we will compare include those under dry conditions (Boujibar et al., 2016; Corgne et al., 2005; Ito et al., 2004) and under wet conditions (Kawamoto, 2004; Nakajima et al., 2019). The results are summarized in **Table 6.**

(Boujibar et al., 2016) starting compositions are 68 wt. % silicate and 32 wt. % metal, with variable sulfur and silicon contents in the metal and an Al_2O_3 content of 2.6 % in the silicate starting composition. (Corgne et al., 2005) contains Al_2O_3 content of 1.96 % in their starting composition, whereas (Ito et al., 2004) have an Al_2O_3 content of 4.26 % in their starting composition. In our case the Al_2O_3 content in the starting composition ranged between 4.6 – 5.0%. Also (Boujibar et al., 2016; Corgne et al., 2005; Ito et al., 2004) started with non-hydrous compositions, and had to raise their samples to a temperature of at least 2000^{o}C in order to obtain melt. In our case, since all our starting compositions contained water, we were able to achieve melt at 1600^{o}C. (Boujibar et al., 2016) use graphite sample capsules in their study, which equilibrates their experiment at a lower oxygen fugacity than in our studies while (Ito et al., 2004) and (Corgne et al., 2005) use rhenium metal capsules which equilibrate their systems at higher fugacity than in our study.

The appropriate partition coefficients from (Boujibar et al., 2016) to compare with our studies are those in which bridgmanite equilibrated with melt near the liquidus and had large melt fractions of ~40%, comparable to those observed in our studies. Unlike in the near-solidus bridgmanite compositions, which had much less melt fractions, no corrections on the EPMA results are necessary.

The aluminum-free Fe partition coefficients in all the studies are the same, irrespective of the initial non-hydrous or hydrous conditions. The Fe partition coefficient, therefore, is not affected by the $Fe^{3+}/\sum Fe$ ratio in bridgmanite, even with change in oxygen fugacity.

In the case of the aluminum-bearing experiments, on the other hand, the $Fe^{3+}/\sum Fe$ ratio in bridgmanite is enhanced by the presence of aluminum. To a first approximation, therefore, we would conclude that the difference might be as a result of the differences in oxygen fugacities. The oxygen fugacity in our study is higher than that in (Boujibar et al., 2016) and lower than in (Corgne et al., 2005) and (Ito et al., 2004), but we obtained the highest Fe partition coefficient in all the experiments. We could therefore conclude that the presence of water may also have contributed to the high Fe partition coefficient.

Meanwhile, when we compare the silica partition coefficients, our Si partition coefficient is on average twice that in all the other three studies conducted under dry conditions. We attribute this primarily to the presence of water. Our results are in good agreement with those by (Kawamoto, 2004), where they carried out hydrous experiments under similar P-T conditions, and also reported the presence of some stishovite. (Kawamoto, 2004) reviewed literature and showed that melts formed from peridotite tend to have a low (Mg + Fe)/Si ratio (more silicic) at low pressures (e.g., (Kushiro, 2001; Mibe et al., 2006; Takahashi, 1986)) whereas (Mg + Fe)/Si ratio becomes higher as pressure increases (e.g., (Mibe et al., 2006; Ohtani, 1987; Takahashi,

1986)). At low pressures, the addition of water *decreases* (Mg + Fe)/Si ratio (more silicic magmas are generated by hydrous melting; (Kushiro, 1972)). In contrast, existing data suggest that at higher pressures (P > 15 GPa), the addition of water *increases* (Mg + Fe)/Si of the melt (e.g., (Kawamoto, 2004; Litasov and Ohtani, 2002)). We found a similar trend in our study: the melt formed by hydrous melting has a higher (Mg + Fe)/Si ratio, leaving SiO_2-enriched residual materials including large crystals of stishovite (**Figure 1 and 5**).

(Nakajima et al., 2019) carried out similar experiments to (Kawamoto, 2004) and reported a broad range of a Si partition coefficients, but at 1600^{o}C their results are approximately what was observed by (Kawamoto, 2004) and in our study. But our results show larger amount of stishovite than these studies. This is presumably due to the difference in the composition of starting materials: our starting materials have higher SiO_2/(MgO + FeO) than Kawamoto (2004) and Nakajima et al. (2019).

Some geophysical implications

Melting in the lower mantle is possible in two cases. First, in the early stage of Earth evolution, magma ocean was likely present. In this case, water content in the melt is small and consequently the results from dry melting experiments (e.g., (Boujibar et al., 2016)) would be applicable. Second, in the later stage of Earth evolution, temperature in the lower mantle is substantially lower than the dry solidus (e.g., (Andrault et al., 2011)), and therefore, partial melting would occur only at the presence of volatiles such as water. Consequently, our results would be applicable to melting that might occur currently in the (shallow) lower mantle that has been suggested by seismological studies (Liu et al., 2016, 2018; Schmandt et al., 2014).

With likely composition determined in the present study, those melts are lighter than the

co-existing minerals and hence migrate upward to the bottom of the mantle transition zone (see also (Karki et al., 2018; Nakajima et al., 2019; Sakamaki, 2017)). This provides a mechanism to keep the mantle transition zone wet (Karato et al., 2020). Because these hydrous melts are less dense than surrounding minerals, they will rise up and eventually be incorporated into the mantle transition zone and change to solid aggregates. These materials will have lower seismic wave velocities than the surrounding typical mantle minerals because these frozen melts are FeO and H_2O rich. Similarly, high FeO and H_2O content also suggest high attenuation. Observed low seismic wave velocity regions in the mantle transition zone (e.g., (Wang et al., 2019)) and low Q regions in the mantle transition zone reported by (Zhu et al., 2013) may be caused by these materials derived from the melts formed in the shallow lower mantle.

In **Figure 9** we compare compositions of residual solids after partial melting under the shallow lower mantle conditions from various studies including (Hart and Zindler, 1986; Javoy et al., 2010; Kawamoto, 2004; Lyubetskaya and Korenaga, 2007a, b; Mcdonough and Sun, 1995; Nakajima et al., 2019; Palme and O'Neill, 2003) where we also include compositions of mid-ocean ridge basalt (MORB) and bulk silicate Earth (BSE). **Figure 9 (a)** is a diagram for SiO_2-rich composition such as bridgmanite or MORB. For MORB composition, silica-rich materials will be formed as a result of melting in the shallow lower mantle. Therefore the amount of stishovite in the deeply subducted oceanic crust will increase after the partial melting in the lower mantle. In contrast, if the initial composition is nearly BSE, the amount of stishovite is much less after partial melting.

Formation of silica-rich materials has possible geochemical and seismological implications. There are some reports of SiO_2 inclusions in diamond of deep mantle origin (e.g., (Kaminsky, 2020)). Given the deep origin, SiO_2 is likely stishovite in the deep mantle but

explaining the presence of pure stishovite is difficult assuming the pyrolytic composition (close to BSE). It is possible that those stishovites are the remnant of lower mantle melting of subducted MORB.

Stishovite itself has not much different seismic wave velocities from other minerals down to ~1200 km, but when stishovite is transported into deeper lower mantle by convection, it will transform to a $CaCl_2$ structure and before the transformation it shows large reduction of C_{12} that causes large seismic anisotropy and reduction in average velocity (shear wave velocity reduction of ~50%, anisotropy in shear velocity exceeding 100 %) (Karki et al., 1997). Consequently, if there is a substantial amount of stishovite, that will cause substantial seismic scattering. Observed seismic scattering in the depth range of 1000 to 1500 km reported by (Kaneshima and Helffrich, 2010) might be due to the presence of stishovite.

Summary and concluding remarks

High-pressure melting experiments were performed for bridgmanite with a range of composition under water-saturated conditions at P = 25 GPa and T = 1600^{o}C equivalent to the shallow lower mantle. We developed a new method of estimating the water content of unquenchable melt via the estimate of the void space in the unquenchable melts. Water (hydrogen) content in the residual solids is determined by FTIR. In most of bridgmanite, there are inclusions of super-hydrous phase B. If these inclusions are formed during cooling water content in hydrous phase B must be included when we estimate water solubility in bridgmanite. Water solubility in the bridgmanite at high pressure and temperature would be ~1000-1500 ppm wt that agrees with the results on inclusion-free bridgmanite reported by (Fu et al., 2019).

However the hypothesis that these inclusions are formed during cooling needs to be tested by further experimental studies.

Our studies confirm some of the earlier studies in showing that the chemical composition of melts formed under high pressure and hydrous conditions are remarkably different from those formed at low pressures. A majority of FeO (and a large fraction of MgO) goes to melt under high-pressure conditions such as the lower mantle conditions. As a consequence, a substantial amount of stishovite is formed in the residual material. The amount of stishovite depends on the composition of the starting materials and is large if the starting material has a MORB-like composition (high FeO/(FeO + MgO) and $Al_2O_3/(Al_2O_3+SiO_2)$). Thus our results provide an explanation for the stishovite paradox discussed by (Kaminsky, 2020). Although the elastic properties of stishovite are not so different from those of other minerals down to ~1000 km, stishovite becomes highly anisotropic and its average velocities become low before the transformation to $CaCl_2$ structure at ~1200 km. This will cause seismic scattering in this depth range.

Acknowledgment

We thank Kanani Lee for helpful insights and discussions, Zhenting Jiang and Jim Eckert for their help with the SEM and EPMA analysis, respectively. This work is supported by the fund from US National Science Foundation grant, EAR-1764271. The authors comply with AGU's data policy, and the data of this study are available from the authors upon request. The authors declare no competing financial interests.

References

Andrault, D., Bolfan-Casanova, N., Lo Nigro, G., Bouhifd, M.A., Garbarino, G., Mezouar, M., 2011. Solidus and liquidus profiles of chondritic mantle: Implications for melting of the Earth across its history. Earth and Planetary Science Letters 304, 251-259.

Balta, J.B., Beckett, J.R., Asimow, P.D., 2011. Thermodynamic properties of alloys of gold-74/palladium-26 with variable amounts of iron and the use of Au-Pd-Fe alloys as containers for experimental petrology. Am Mineral 96, 1467-1474.

Baron, M.A., Lord, O.T., Myhill, R., Thomson, A.R., Wang, W., Tronnes, R.G., Walter, M.J., 2017. Experimental constraints on melting temperatures in the MgO-SiO2 system at lower mantle pressures. Earth and Planetary Science Letters 472, 186-196.

Bolfan-Casanova, N., Keppler, H., Rubie, D.C., 2003. Water partitioning at 660 km depth and evidence for very low water solubility in magnesium silicate perovskite. Geophysical Research Letters 30, 10.1029/2003GL017182.

Bolfan-Casanova, N., Mackwell, S.J., Keppler, H., McCammon, C., Rubie, D.C., 2002. Pressure dependence of H solubility in magnesiowüstite up to 25 GPa: implications for the storage of water in the Earth's lower mantle. Geophysical Research Letters 29, 89-81/89-84.

Boujibar, A., Bolfan-Casanova, N., Andrault, D., Bouhifd, M.A., Trcera, N., 2016. Incorporation of Fe2+ and Fe3+ in bridgmanite during magma ocean crystallization. Am Mineral 101, 1560-1570.

Braterman, P.S., Cygan, R.T., 2006. Vibrational spectroscopy of brucite: A molecular simulation investigation. Am Mineral 91, 1188-1196.

Corgne, A., Liebske, C., Wood, B.J., Rubie, D.C., Frost, D.J., 2005. Silicate perovskite-melt partitioning of trace elements and geochemical signature of a deep perovskitic reservoir. Geochimica Et Cosmochimica Acta 69, 485-496.

Cynn, H., Hofmeister, A.M., Burnley, P.C., Navrotsky, A., 1996. Thermodynamic properties and hydrogen speciation from vibrational spectra of dense hydrous magnesium silicates. Phys Chem Miner 23, 361-376.

de Oliveira, E.F., Hase, Y., 2001. Infrared study and isotopic effect of magnesium hydroxide. Vib Spectrosc 25, 53-56.

Fu, S., Yang, J., Karato, S., Vasiliev, A., Presniakov, M.Y., Gavrilliuk, A.G., Ivanova, A.G., Hauri, E.H., Okuchi, T., Prevjav, N., Lin, J., 2019. Water Concentration in Single - Crystal (Al,Fe) - Bearing Bridgmanite Grown From the Hydrous Melt: Implications for Dehydration Melting at the Topmost Lower Mantle. Geophysical Research Letters 46.

Grove, T.L., 1981. Use of Fept Alloys to Eliminate the Iron Loss Problem in 1-Atmosphere Gas Mixing Experiments - Theoretical and Practical Considerations. Contrib Mineral Petr 78, 298-304.

Gudmundsson, G., Holloway, J.R., 1993. Activity-Composition Relationships in the System Fe-Pt at 1300-Degrees-C and 1400-Degrees-C and at 1-Atm and 20-Kbar. Am Mineral 78, 178-186.

Hart, S.R., Zindler, A., 1986. In Search of a Bulk-Earth Composition. Chem Geol 57, 247-267.

Hemley, R.J., Jephcoat, A.P., Mao, H.K., Zha, C.S., Finger, L.W., Cox, D.E., 1987. Static Compression of H2O-Ice to 128 GPa (1.28 Mbar). Nature 330, 737-740.

Hernandez, E.R., Alfe, D., Brodholt, J., 2013. The incorporation of water into lower-mantle perovskites: A first-principles study. Earth and Planetary Science Letters 364, 37-43.

Hirschmann, M.M., Tenner, T., Aubaud, C., Withers, A.C., 2009. Dehydration melting of nominally anhydrous mantle: The primacy of partitioning. Phys Earth Planet In 176, 54-68.

Irifune, T., Shinmei, T., McCammon, C.A., Miyajima, N., Rubie, D.C., Frost, D.J., 2010. Iron partitioning and density changes of pyrolite in Earth's lower mantle. Science 327, 193-195.

Ito, E., Kubo, A., Katsura, T., Walter, M.J., 2004. Melting experiments of mantle materials under lower mantle conditions with implications for magma ocean differentiation. Phys Earth Planet In 143, 397-406.

Ito, E., Takahashi, E., 1987. Melting of peridotites at uppermost lower-mantle conditions. Nature 328, 514-517.

Javoy, M., Kaminski, E., Guyot, F., Andrault, D., Sanloup, C., Moreira, M., Labrosse, S., Jambon, A., Agrinier, P., Davaille, A., Jaupart, C., 2010. The chemical composition of the Earth: Enstatite chondrite models. Earth and Planetary Science Letters 293, 259-268.

Kaminsky, F., 2020. Basic problems concerning the composition of the Earth's lower mantle. Lithos 364-365, 105515.

Kaneshima, S., Helffrich, G., 2010. Small scale heterogeneity in the mid-lower mantle beneath the circum-Pacific area. Physics of the Earth and Planetary Interiors 183, 91-103.

Karato, S., Park, J., Karki, B.B., 2020. Deep mantle melting, global water circulation and its implications for the stability of the ocean mass. Progress in Earth and Planetary Science 7, 76.

Karki, B.B., Ghosh, D.B., Maharjan, C., Karato, S., Park, J., 2018. Density-pressure profiles of Fe-bearing $MgSiO_3$ liquid: Effects of valence and spin states, and implications for the chemical evolution of the lower mantle. Geophysical Research Letters 45, 3959-3966.

Karki, B.B., Stixrude, L., Crain, J., 1997. Ab initio elasticity of three high-pressure polymorphs of silica. Geophysical Research Letters 24, 3269-3272.

Kawamoto, T., 2004. Hydrous phase stability and partial melt chemistry in H_2O-saturated KLB-1 peridotite up to the uppermost lower mantle conditions. Physics of Earth and Planetary Interiors 143/144, 387-395.

Kessel, R., Beckett, J.R., Stolper, E.M., 2001. Thermodynamic properties of the Pt-Fe system. Am Mineral 86, 1003-1014.

Koch-Muller, M., Dera, P., Fei, Y., Hellwig, H., Liu, Z., Van Orman, J., Wirth, R., 2005. Polymorphic phase transition in Superhydrous Phase B. Phys Chem Miner 32, 349-361.

Kohlstedt, D.L., Mackwell, S.J., 1998. Diffusion of hydrogen and intrinsic point defects in olivine. Zeitschrift für Phisikalische Chemie 207, 147-162.

Kushiro, I., 1972. Effect of water on composition of magmas formed at high pressures. Journal of Petrology 13, 71-136.

Kushiro, I., 2001. Partial melting experiments on peridotite and origin of mid-ocean ridge basalt. Annual Review of Earth and Planetary Sciences 29, 71-107.

Litasov, K., Ohtani, E., 2002. Phase relations and melt compositions in CMAS-pyrolite-H2O system up to 25 GPa. Phys Earth Planet In 134, 105-127.

Litasov, K., Ohtani, E., Langenhorst, F., Yurimoto, H., Kubo, T., Kondo, T., 2003. Water solubility in Mg-perovskites, and water storage capacity in the lower mantle. Earth and Planetary Science Letters 211, 189-203.

Litasov, K.D., Kagi, H., Shatskiy, A., Ohtani, E., Lakshtanov, D.L., Bass, J.D., Ito, E., 2007. High hydrogen solubility in Al-rich stishovite and water content in the lower mantle. Earth and Planetary Science Letters 262, 620-634.

Liu, L.G., Lin, C.C., Mernagh, T.P., Inoue, T., 2002. Raman spectra of phase C (superhydrous phase B) at various pressures and temperatures. Eur J Mineral 14, 15-23.

Liu, Z., Park, J., Karato, S., 2016. Seismological detection of low velocity anomalies surrounding the mantle transition zone in Japan subduction zone. Geophysical Research Letters 43, 2480-2487.

Liu, Z., Park, J., Karato, S., 2018. Seismic evidence for water transport out of the mantle transition zone beneath the European Alps. Earth and Planetary Science Letters 482, 93-104.

Lyubetskaya, T., Korenaga, J., 2007a. Chemical composition of Earth's primitive mantle and its variance: 1. Method and results. J Geophys Res-Sol Ea 112.

Lyubetskaya, T., Korenaga, J., 2007b. Chemical composition of Earth's primitive mantle and its variance: 2. Implications for global geodynamics. J Geophys Res-Sol Ea 112.

Mcdonough, W.F., Sun, S.S., 1995. The Composition of the Earth. Chem Geol 120, 223-253.

Meade, C., Reffner, J.A., Ito, E., 1994. Synchrotron infrared absorbency measurements of hydrogen in MgSiO3 perovskite. Science 264, 1558-1560.

Mibe, K., Fujii, T., Yasuda, A., Ono, S., 2006. Mg-Fe partitioning between olivine and ultramafic melts at high pressures. Geochemica et Cosmochemica Acta 70, 757-766.

Murakami, M., Hirose, K., Yurimoto, H., Nakashima, S., Takafuji, N., 2002. Water in Earth's lower mantle. Science 295, 1885-1887.

Nakajima, A., Sakamaki, T., Kawazoe, T., Suzuki, A., 2019. Hydrous magnesium-rich magma genesis at the top of the lower mantle. Sci Rep-Uk 9.

Nishiyama, N., Yagi, T., 2003. Phase relation and mineral chemistry in pyrolite to 2200^{o}C under the lower mantle pressures and implications for dynamics of mantle plumes. Journal of Geophysical Research 108, 10.1029/2002JB002216.

Nomura, R., Ozawa, H., Tateno, S., Hirose, K., Hernlund, J., Muto, S., Ishii, H., 2011. Spin crossover and iron-rich silicate melt in the Earth's deep mantle. Nature 473, 199-203.

Ohtani, E., 1987. Ultrahigh-pressure melting of a model chondritic mantle and pyrolite compositions, in: M.H. Manghani, a.Y.S. (Ed.), High-Pressure Research in Mineral Physics. Terra Scientific Publishing Company, Tokyo, pp. 87-93.

Ohtani, E., 2005. Recent progress in experimental mineral physics: Phase relations of hydrous systems and the role of water in slab dynamics. Earth's Deep Mantle: Structure, Composition, and Evolution 160, 321-334.

Ohtani, E., Litasov, K., Hosoya, T., Kubo, T., Kondo, T., 2004. Water transport into the deep mantle and formation of a hydrous transition zone. Physics of the Earth and Planetary Interior 143/144, 255-269.

591 Palme, H., O'Neill, H.S.C., 2003. Cosmochemical estimates of mantle composition, Treatise on
592 Geochemistry. Elsevier, New-York, pp. pp. 1–38.

593 Panero, W.R., Piggot, J.S., Reaman, D.M., Kabbes, J.E., Zhenxian, L., 2015. Dry (Mg,Fe)SiO3
594 perovskite in the Earth's lower mantle.

595 Panero, W.R., Thomas, C., Myhill, R., Piggot, J.S., 2020. Dehydration melting below the
596 undersaturated transition zone. Geochemistry, Geophysics, Geosystems 21.

597 Paterson, M.S., 1982. The determination of hydroxyl by infrared absorption in quartz, silicate
598 glasses and similar materials. Bulletin Mineral 105, 20-29.

599 Pawley, A.R., Mcmillan, P.F., Holloway, J.R., 1993. Hydrogen in Stishovite, with Implications
600 for Mantle Water-Content. Science 261, 1024-1026.

601 Rubie, D.C., Karato, S., Yan, H., O'Neill, H.S.C., 1993. Low differential stress and controlled
602 chemical environment in multianvil high-pressure experiments. Physics and Chemistry of
603 Minerals 20, 315-322.

604 Sakamaki, T., 2017. Density of hydrous magma. Chemical Geology 475, 135-139.

605 Schmandt, B., Jacobsen, S.D., Becker, T.W., Liu, Z., Dueker, K.G., 2014. Dehydration melting
606 at the top of the lower mantle. Science 344, 1265-1268.

607 Takahashi, E., 1986. Melting of a dry peridotite KLB-1 up to14 GPa: implications on the origin
608 of peridotitic upper mantle. Journal of Geophysical Research 91, 9367-9382.

609 Vanderlaan, S.R., Vangroos, A.F.K., 1991. Pt-Fe Alloys in Experimental Petrology Applied to
610 High-Pressure Research on Fe-Bearing Systems. Am Mineral 76, 1940-1949.

611 Wang, Y., Pavlis, G.L., Li, M., 2019. Heterogeneous distribution of water in the mantle
612 transition zone inferred from wavefield imaging. Earth and Planetary Science Letters 505, 42-50.

613 Wood, B.J., 2000. Phase transformations and partitioning relations in peridotite under lower
614 mantle conditions. Earth and Planetary Science Letters 174, 341-354.

615 Zhu, H., Bozdag, E., Duffy, T.S., Tromp, J., 2013. Seismic attenuation beneath Europe and
616 North Atlantic: implications for water in the mantle. Earth and Planetary Science Letters 381, 1-
617 11.
618

Table 1. Starting Compositions of synthesized hydrous bridgmanite (in wt. %), (Mg + Fe)/Si ratios and expected stoichiometry of phase(s).

Starting materials (Run number)	**MgO**	**$Mg(OH)_2$**	**SiO_2**	**Al_2O_3**	**FeO**	**(Mg + Fe)/Si (mole ratio)**	**Initial water content***
Pure $MgSiO_3$ Bridgmanite. Excess SiO_2 (**K994**)	24.0	17.0	59.0	0.0	0.0	0.90	5 wt. % H_2O
Pure $MgSiO_3$ Bridgmanite. Excess MgO (**K1073, K1077**)	22.0	33.0	45.0	0.0	0.0	1.48	10 wt. % H_2O
Al- Bearing $MgSiO_3$ Bridgmanite (**K1098**)	14.5	32.0	49.5	4.0	0.0	1.10	10 wt. % H_2O
Fe- Bearing $MgSiO_3$ Bridgmanite (**K1157**)	11.0	32.0	47.0	0.0	10.0	1.23	10 wt. % H_2O
Al- and Fe – Bearing $MgSiO_3$ Bridgmanite (**K1161**)	11.0	32.0	47.0	5.0	5.0	1.14	10 wt. % H_2O
Al- and Fe – Bearing Bridgmanite (**K1182, 1217, 1222**)	8.9	32.0	46.7	4.6	7.2	1.12	10 wt. % H_2O

* Water content was calculated from brucite

624

625 **Table 2.** Composition of run products (hydrous bridgmanite (Bdg), stishovite (St) and melt) in wt. %.

	K1077 $MgSiO_3$		K1098 $(Mg, Al)SiO_3$		K1157 $(Mg, Fe)SiO_3$			K1161 $(Mg, Al, Fe)SiO_3$			K1182 $(Mg, Al, Fe)SiO_3$		K1222 $(Mg, Al, Fe)SiO_3$	
	Bdg	**Melt**	**Bdg**	**Melt**	**Bdg**	**St**	**Melt**	**Bdg**	**St**	**Melt**	**St**	**Melt**	**St**	**Melt**
MgO	43.4	41.6	30.1	27.8	36.5	0.0	31.6	35.9	0.1	35.2	0.0	26.9	0.0	26.5
SiO_2	63.4	35.4	47.8	21.5	56.7	97.8	22.6	53.1	94.1	27.3	93.2	13.4	88.4	13.4
Al_2O_3	0.1	0.1	18.0	0.6	0.0	0.0	0.0	4.2	1.6	3.5	3.0	4.7	2.8	5.2
FeO	0.0	1.0	0.0	0.01	5.0	0.1	17.2	5.4	0.2	5.1	0.1	18.3	0.0	16.9
Oxide totals	**105.8**	**77.2**	**96.0**	**49.9**	**98.2**	**98.0**	**71.6**	**98.7**	**95.9**	**71.5**	**96.3**	**63.2**	**91.3**	**62.0**
Mg	2.0	2.5	1.6	2.6	1.9	0.0	2.2	1.9	0.0	2.4	0.0	2.2	0.0	2.2
Si	2.0	1.5	1.7	1.4	2.0	3.0	1.1	1.8	2.9	1.2	2.9	0.7	2.9	0.7
Al	0.0	0.0	0.7	0.1	0.0	0.0	0.0	0.2	0.1	0.2	0.1	0.3	0.1	0.3
Fe	0.0	0.0	0.0	0.0	0.1	0.0	0.7	0.2	0.0	0.2	0.0	0.8	0.0	0.8
Cations per 6 O	4	4	4	4	4	3	4	4	3	4	3	4		4
(Mg + Fe)/Si	1.0	1.8	0.9	1.9	1.0		2.7	1.1		2.0		4.2		4.0

626

627

628

629 **Table 3**: Porosity estimation and calculated water measurement results from starting water contents

Composition (Experiment number)	Starting Water Content (wt. %)	Porosity (%)	Wt. % water in melt				
			0 GPa	5 GPa	10 GPa	25 GPa	100 – EPMA Total
$MgSiO_3$ (K1003)	5	16	7.8	8.8	9.4	10.4	-
$MgSiO_3$ (K1077)	5	15	7.4	8.4	8.9	9.9	22.8
(Mg, Al, Si)O_3 (K1098)	10	21	10.6	11.9	12.7	14.1	50.1
(Mg, Fe, Si)O_3 (K1157)	10	18	8.7	9.8	10.5	11.6	28.4
(Mg, Al, Fe, Si)O_3 (K1217)	10	18	9.1	10.2	10.9	12.1	-
(Mg, Al, Fe, Si)O_3 (K1222)	10	19	9.6	10.9	11.6	12.8	38.0
(Mg, Al, Fe, Si)O_3 (K1270)	5	16	7.8	8.8	9.4	10.4	-
$MgSiO_3$ (K1279)	1	4	1.9	2.2	2.4	2.6	-
$MgSiO_3$ (K1283)	0.1	2	1.0	1.1	1.2	1.4	-
$MgSiO_3$ (K1298)	3	3	1.5	1.7	1.8	2.0	-

630

631

Table 4: Summary of the FTIR peak positions in the different bridgmanite compositions studied

Composition (Experiment number)	**Wavenumber cm^{-1}**					
$MgSiO_3$ (K994)					3446	3697
(Mg, Al, Si)O_3 (K1098)			3346	3405		3695
(Mg, Fe, Si)O_3 (K1157)		3296	3394			3687
(Mg, Al, Fe, Si)O_3 (K1161)	3109	3242	3351	3402	3479	3690

638

639

640 **Table 5**: Fe mass balance analysis of sample K1157 using EPMA results given in **Table 2**

641

Wt. % of Initial FeO	Wt. % FeO in Bdg	Wt. % FeO in Melt	Vol. % Bdg	Vol. % Melt	Total Fe
10	*5.0	*17.2	60	40	
Wt. % of Initial Fe	Wt. % Fe in Bdg	Wt. % Fe in Melt	Wt. % of Fe in Bdg	Wt. % of Fe in Melt	
7.8	3.9	13.4	2.3	5.7	7.7
				% Iron Loss	1.30

642

643 *EPMA measurements are given in FeO content

644

Table 6: A comparison on FeO and Al_2O_3 partition coefficient between bridgmanite and co-existing melt

$K_D^{Fe(Si)}$ is defined as $K_D^{Fe(Si)} = \frac{(Fe(Si)/Mg)_{bridgmanite}}{(Fe(Si)/Mg)_{melt}}$

Reference / **Experimental Conditions** / **Partition Function**	**(Boujibar et al., 2016)**		**(Ito et al., 2004)**	**(Corgne et al., 2005)**	**(Kawamoto, 2004)**	**(Nakajima et al., 2019)**	**This Study**
	25 GPa 1900 - 2050°C Graphite cap. Dry conditions		31 GPa 2500°C Rhenium cap. Dry conditions	25 GPa 2350°C Rhenium cap. Dry conditions	24 GPa 1400°C Gold cap. Wet conditions	23.5 – 26 GPa 1300 – 1600 °C Gold cap. Wet conditions	25 GPa 1600°C Platinum cap. Wet conditions
	Near liquidus	Near solidus	Near solidus				
K_D^{Si} Al-Bearing	1.10	1.10	1.26	-	1.98	2.43 - 4.36	2.05
K_D^{Si} Al-Free	1.22	1.10	-	1.15	-	-	1.69
K_D^{Fe} Al-Bearing	0.30	1.10	0.42	0.37	0.69	1.13	1.05
K_D^{Fe} Al-Free	0.27	1.10	-	0.26	-	-	0.25

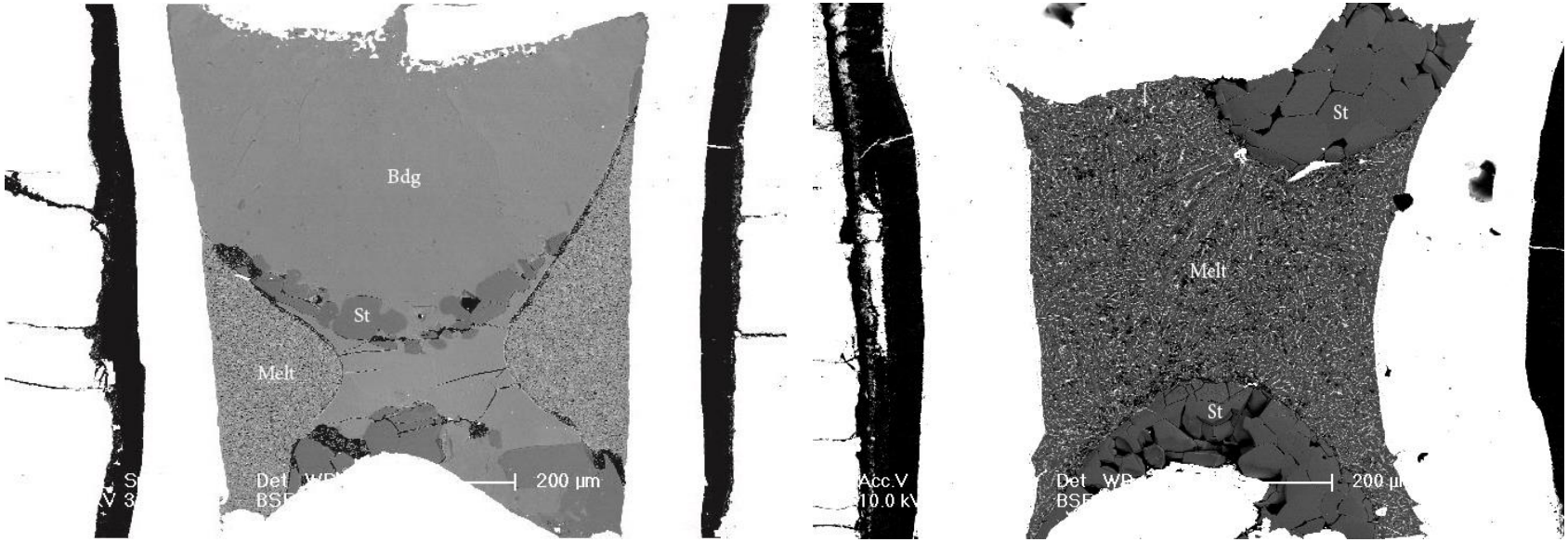

Figure 1. Back-scattered electron SEM images of a polished MgO-SiO_2-FeO-H_2O system containing ~10 wt. % H_2O in the starting mixture (K1157; **left**), and MgO-SiO_2-FeO-Al_2O_3-H_2O system containing ~10 wt. % H_2O in the starting mixture (K1182; **right**). Bridgmanite (Bdg), stishovite (St) and melt regions are labeled. The scale bars are 200 µm. See **Table 1** for sample compositions and **Table 2** for synthesis conditions.

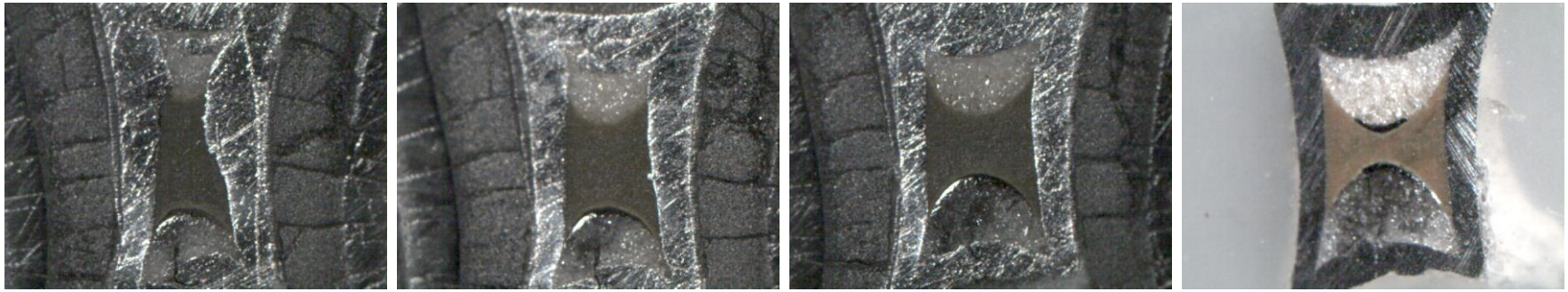

0.811 mm 0.680 mm 0.509 mm 0.361 mm

Figure 2. Optical images of a sample after successive polishing for melt fraction analysis. Also shown are the total sample thickness at each stage of polishing. Roughly each polishing step removed 200 micron (K1217).

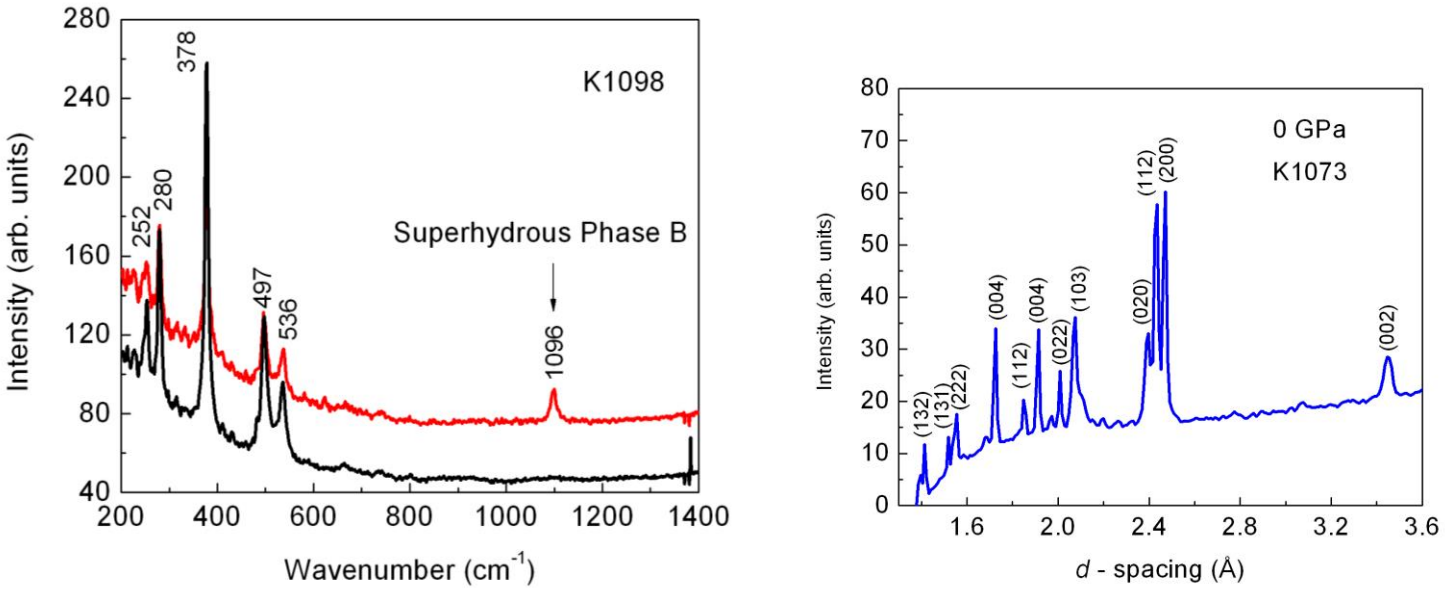

Figure 3. Raman spectra of Mg, Al - bearing bridgmanite, K1098, at two different locations at ambient conditions. The red curve is from a region containing an inclusion showing evidence for a superhydrous phase B inclusion. X-ray diffraction spectra on left from pure $MgSiO_3$ bridgmanite crystal collected from assemblage showing bridgmanite structure.

673

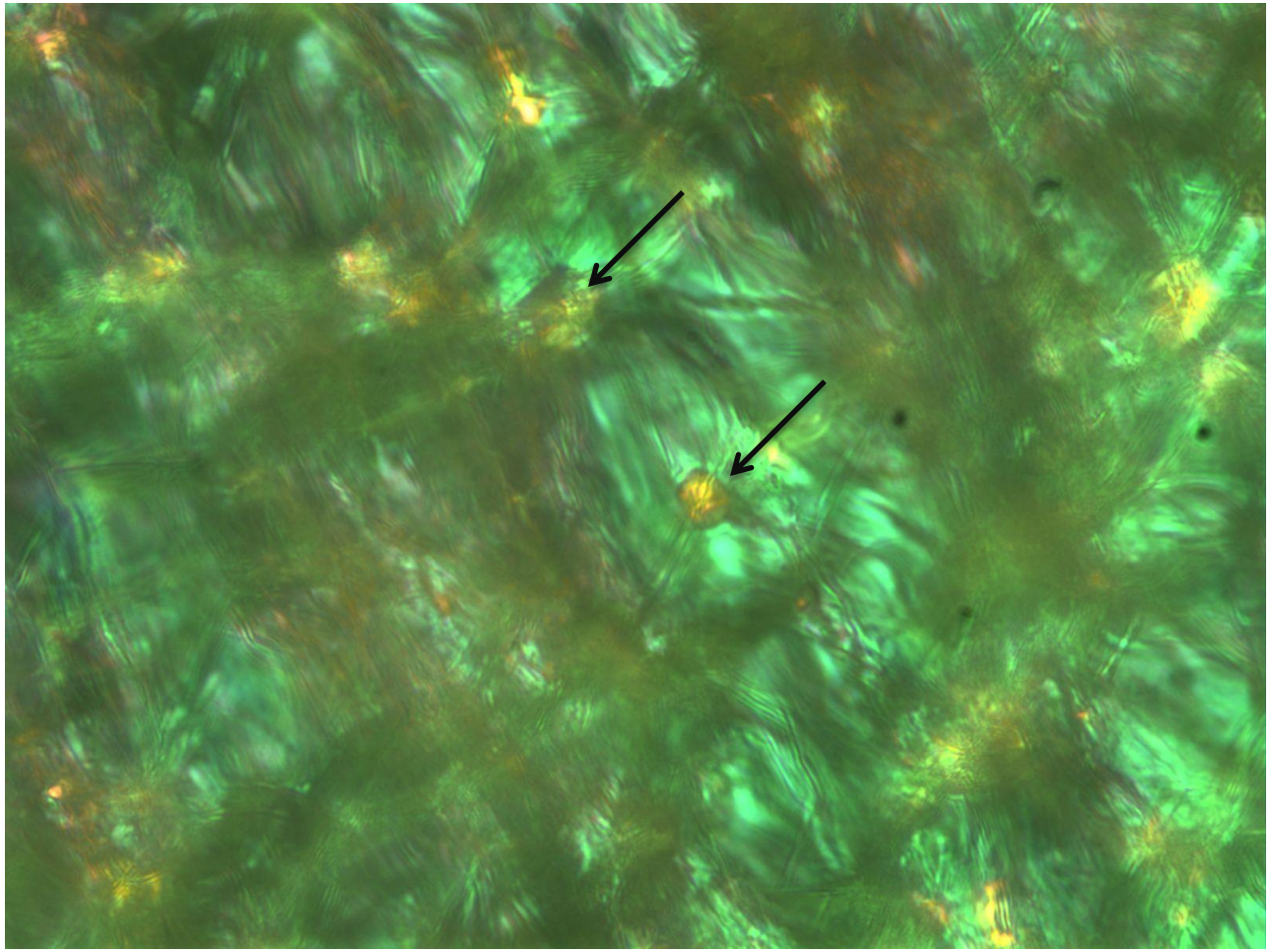

674 **Figure 4:** Superhydrous Phase B inclusions in (Mg, Al, Si)O_3-bridgmanite (K1098)

675

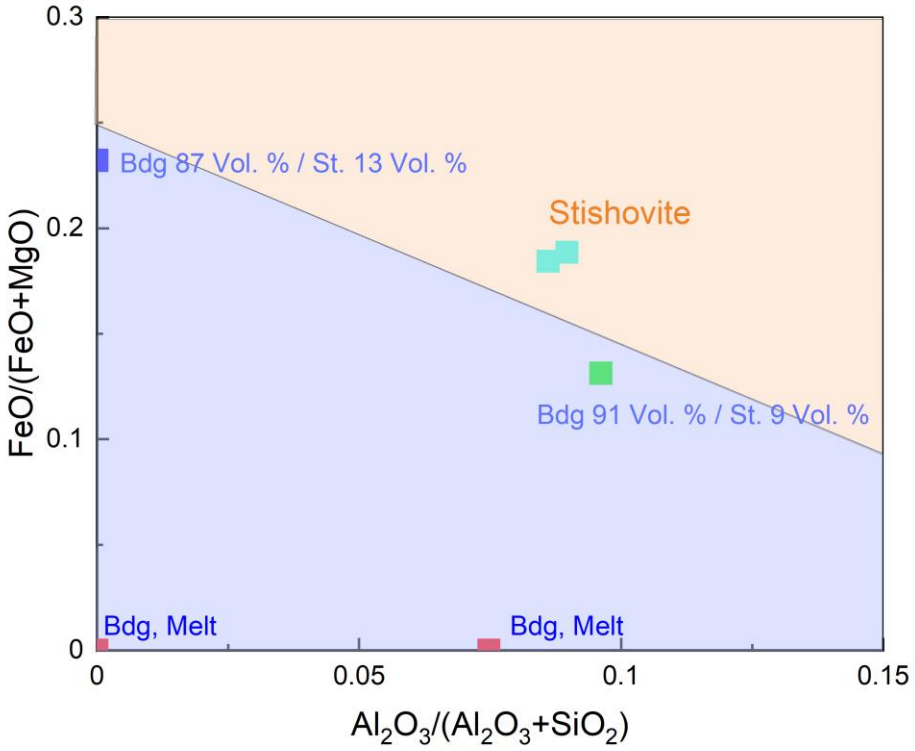

Figure 5: Diagram showing the mineralogy of the residual solids for the different starting compositions. Amount of stishovite depends strongly on the composition of the starting material.

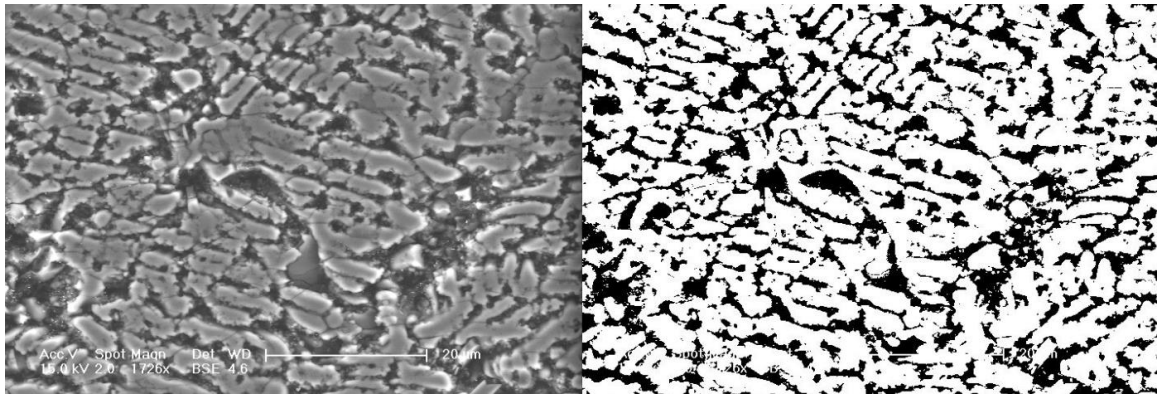

K1077 5% Wt. H2O

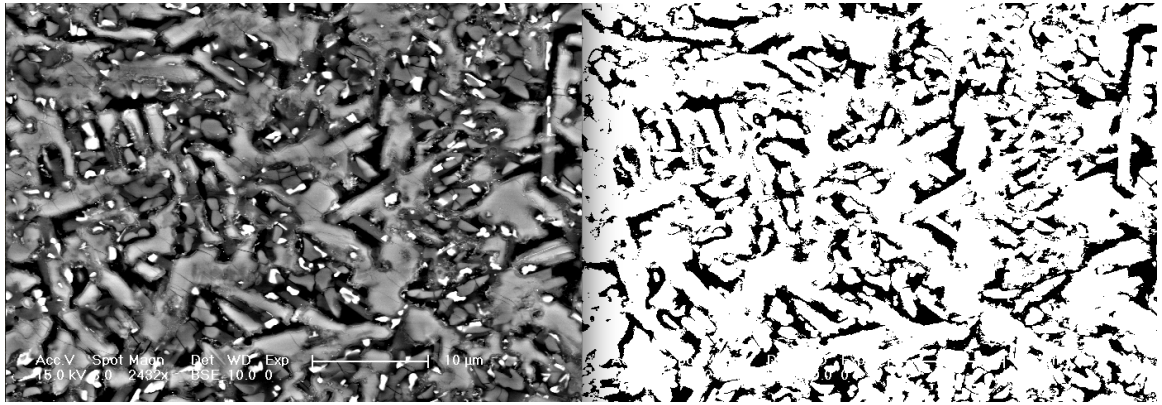

K1157 10% Wt. H2O

Figure 6: SEM photo micrographs of "quenched" melt. Melt is not quenched but those regions show a mixture of crystals and voids. We estimated the water content in the melt from the void space as explained in the text.

687

(a) (b)

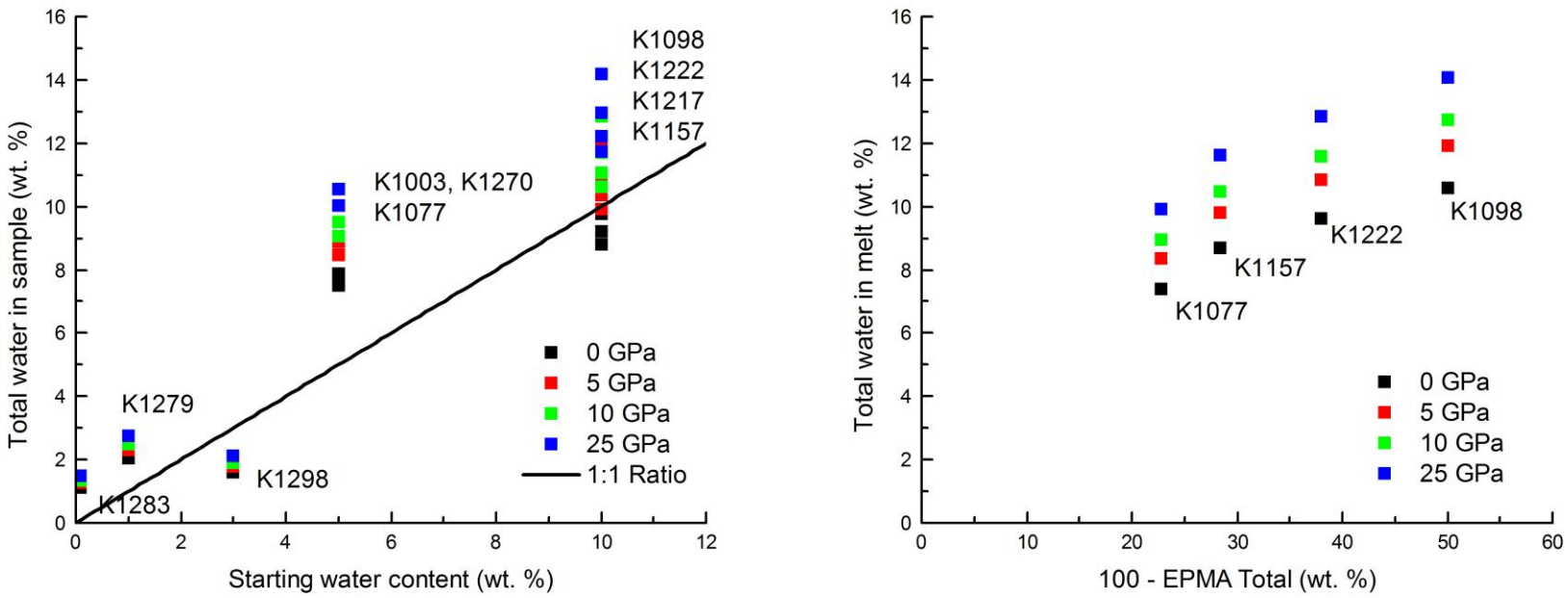

688

689 **Figure 7**: (a) A comparison of the water content in the samples with the initial water content, calculated from the void space and
690 bridgmanite water content, (b) Comparison of the water content in the melt calculated from the porosity with that determined as less
691 than 100% of the total of the oxides from EPMA measurement.

692

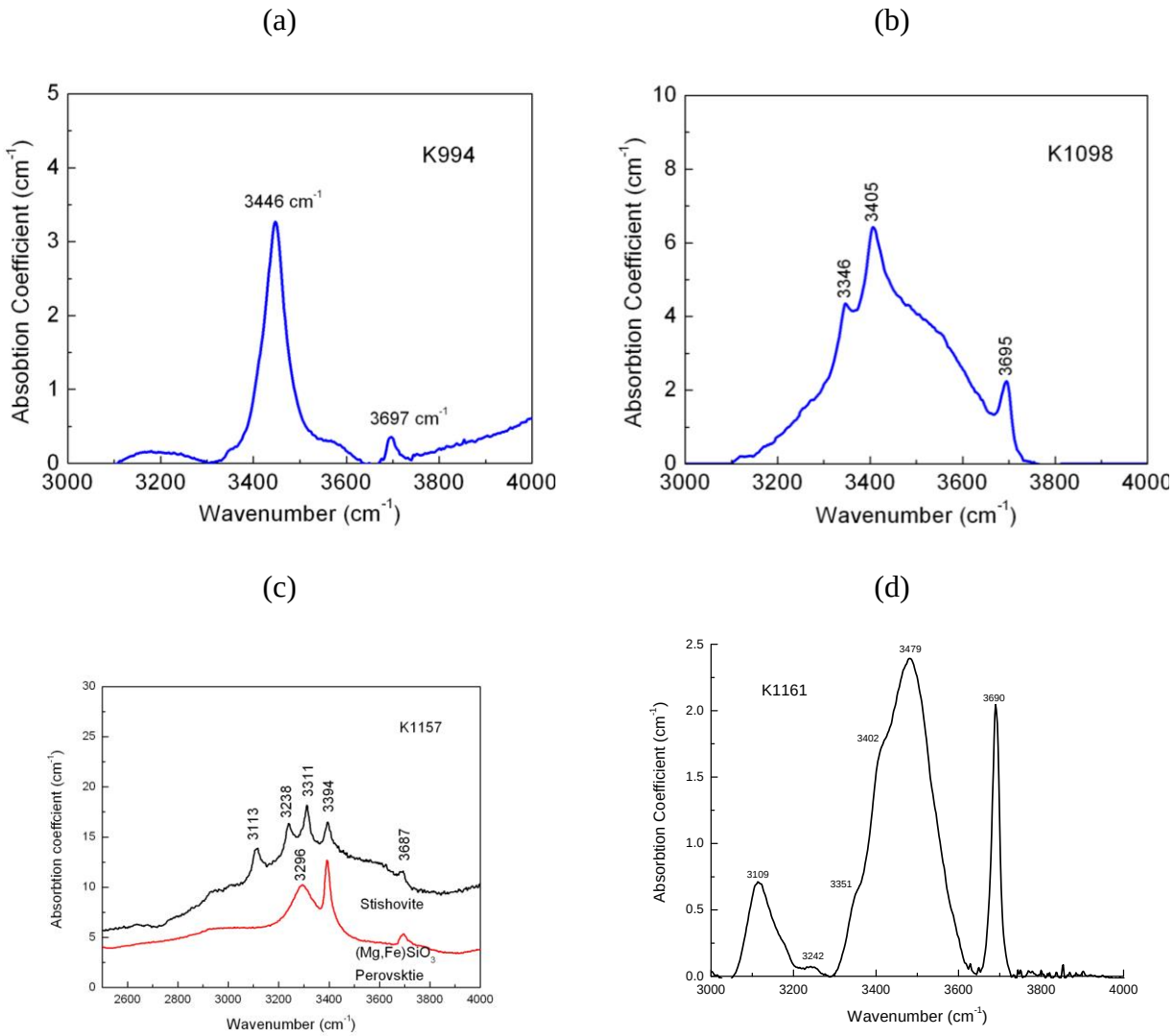

Figure 8: FTIR spectra of the bridgmanite compositions (a) Fe-Al free bridgmanite (K994) (b) Al-bearing bridgmanite (K1098). The peaks are attributed to superhydrous B. The peak at 3695 cm^{-1} may also be attributed to brucite. (c) K1157. The black spectrum shows absorption peaks from the stishovite phase while the red, shows the absorption peaks from (Mg, Fe, Si)O_3 bridgmanite phase. **(d)** (Mg, Fe, Al)SiO_3 **(e)** K1182. Both peaks at 2661 cm^{-1} and 3128 cm^{-1} wavenumbers are from stishovite.

693

(a) (b)

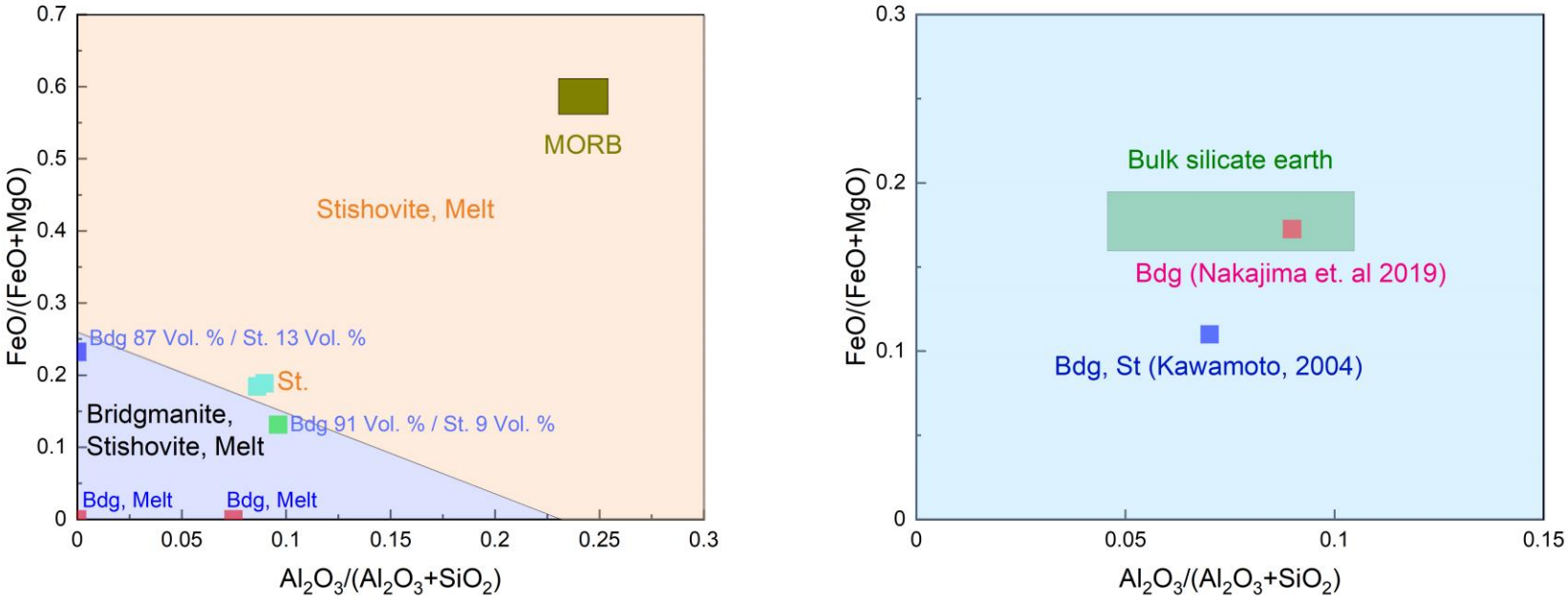

694 **Figure 9**: Composition of residual solids after partial melting under "wet" shallow lower mantle conditions.

695 (**a**) Results for which starting material is bridgmanite (MORB-like composition) and (**b**) Results for which the starting material has

696 bulk silicate Earth composition.